Rayko Simura*, Shohei Kawai and Kazumasa Sugiyama

Phase Transition and Thermal Expansion of $Ba_3RB_3O_9$ (R = Sm–Yb, and Y)

DOI 10.1515/htmp-2015-0290
Received August 20, 2015; accepted February 6, 2016

Abstract: High temperature powder X-ray diffraction measurements of $Ba_3RB_3O_9$ (R = Sm–Yb, and Y) were carried out at temperatures ranging from room temperature to just below the corresponding melting temperatures (1,200–1,300 °C). No phase transition was found for the H-type phase ($R\bar{3}$) with R = Sm–Tb and the L-type phase ($P6_3$ cm) with R = Tm–Yb. On the other hand, phase transition from the L phase to the H phase was observed for R = Dy–Er, and Y at around 1,100–1,200 °C. The obtained axial thermal expansion coefficient (ATEC) of the a-axis was larger than that of the c-axis for the H phase, and the ATEC of the c-axis was larger than that of the a-axis for the L phase. The observed anisotropic nature of ATEC is attributed to the distribution of the BO_3 anionic group with rigid boron–oxygen bonding in the structures of the H and L phases.

Keywords: borates, phase transition, thermal expansion, X-ray diffraction, high temperature

PACS® (2010). Thermal expansion, 65.40.De, Crystal structure inorganic compounds, 61.66.Fn

Introduction

The $Ba_3RB_3O_9$ (R = rare earth element; REE) systems show two polymorphs corresponding to the type of REE. One is the H-type structure with the space group $R\bar{3}$ in the case of lighter REEs (R = Nd–Dy) (Figure 1(a)), and the other is the L-type structure with the space group $P6_3$ cm reported for heavier REEs (R = Dy–Lu, and Y) (Figure 1(b)) [1–5]. The H-type structure of $Ba_3RB_3O_9$ is a potential host material for non-linear optical, laser, and scintillator application [6–10]. In particular, H-type compounds with Gd, Lu, or Y as the REE attract much interest as a potential host crystal in optical applications, because the elements generally produce no unfavorable photoluminescence. In addition to the structural variation associated with the REE, the phase transition as a function of temperature was reported in systems with the middle rare earth elements and Y. For the practical use of the H-type structure, knowledge of the detailed conditions of chemistry and temperature for the phase stability in the $Ba_3RB_3O_9$ systems, and the corresponding physical properties such as the thermal expansion coefficient, is strongly required. This prompted us to conduct a systematic study of $Ba_3RB_3O_9$ compounds (R = Sm–By, and Y) with respect to their structure and high temperature behaviors. High temperature X-ray diffraction measurements were performed to confirm the crystal structural change and to clarify the axial thermal expansion coefficients (ATECs) of the H and L phases in the $Ba_3RB_3O_9$ systems (R = Sm–Yb, and Y).

***Corresponding author: Rayko Simura,** Institute for Materials Research, Tohoku University, 2-1-1 Katahira, Aoba-ku, Sendai, Miyagi 980–8577, Japan, E-mail: ray@imr.tohoku.ac.jp
Shohei Kawai, Kazumasa Sugiyama, Institute for Materials Research, Tohoku University, 2-1-1 Katahira, Aoba-ku, Sendai, Miyagi 980–8577, Japan

Experimental

Sample preparation

Sample powders of $Ba_3RB_3O_9$ compounds (R = Sm–Yb, and Y) were prepared by the high-temperature solid-state reaction. Stoichiometric mixtures of raw chemicals (4N R_2O_3, 3N $BaCO_3$, and 3N H_3BO_3) were ground together and subsequently molded into pellets. Then, they were placed in alumina crucibles and sintered for 24 h at 1,000 °C in a muffle furnace. After the furnace was cooled down to room temperature (RT; 27 °C), the sintered pellets were crushed into powders for the following measurements.

Thermal analysis

Thermogravimetry-differential thermal analyses (TG-DTA) were performed for the prepared sample powders from RT to 1,350 °C using Pt pans with a Rigaku TG8120. Heating and cooling rates were 20 K/min. The obtained melting temperature was used for determining the temperature range for the high temperature powder X-ray diffraction (HT-XRD) measurements.

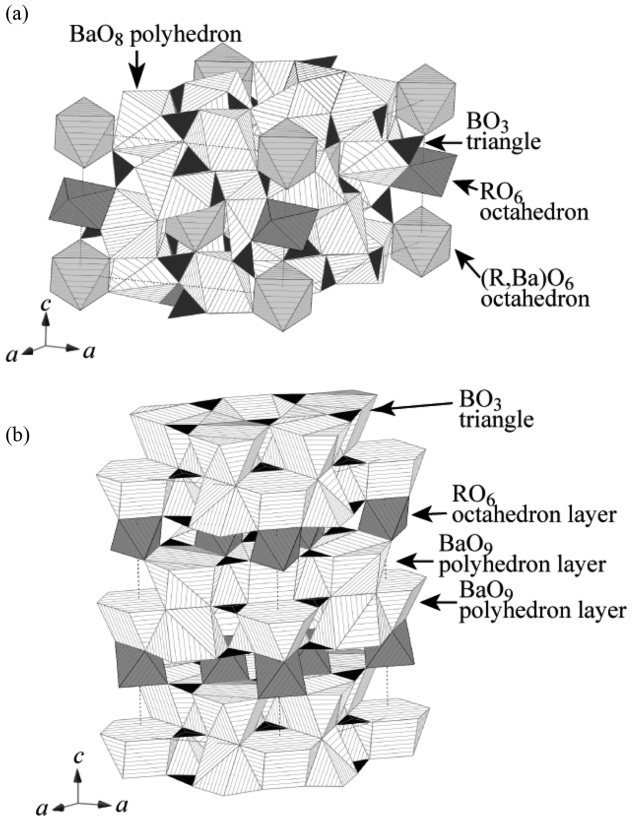

Figure 1: Schematic illustration of the crystal structures of the (a) H phase and (b) L phase. Oxygen-coordinated polyhedrons of cations (R = REE), Ba, and B) are drawn. The H phase is constructed of BO_3 triangles, BaO_8 polyhedrons, (Ba,R)O_6 octahedrons, and RO_6 octahedrons. The L phase is composed of three types of alternating layers; BO_3 triangles, BaO_9 polyhedrons, and RO_6 octahedrons.

X-ray diffraction measurements

The HT-XRD measurements utilized the ordinary Bragg-Brentano optics, a diffracted-beam monochromator, and Cu $K\alpha$ radiation. An electric furnace with a water-cooling device was placed at the center of a two-axes goniometer (Ultima III, Rigaku), and the temperature of the furnace was controlled using a R-type thermocouple. The temperature at the sample was calibrated using the result of high temperature X-ray diffraction for Al_2O_3 powder and the published standard data [11]. Temperatures of HT-XRD measurements during the heating period were set at RT, 200 °C, 400 °C, 600 °C, 800 °C, and 1,000 °C. In particular, intervals of 50 °C or 100 °C were also selected from 1,000 °C to the melting temperatures. For the cooling-down period over 800 °C, the HT-XRD measurements were performed at similar temperatures. In order to stabilize the temperature at the sample, HT-XRD measurements were started 5 min after reaching the target temperature. In our HT-XRD measurements, the heating rate was set at 10 K/min below 1,000 °C and 5 K/min above 1,000 °C, and the cooling rate was set at 20 K/min.

Unit cell parameters were calculated by the least-square refinement with the computer program JADE ver. 6.5. The variations of the obtained unit cell parameters were analyzed using a quadratic function ($L = L_0 + L_1T + L_2T^2$, where L = the values of a or c axis, T = temperature (°C), and L_0, L_1, and L_2 are coefficients). The obtained coefficients are summarized in Table 1. ATEC ($\alpha_T = 1/L_0$

Table 1: The fitted coefficients for the quadratic curve shown in Figure 5 ($L = L_0 + L_1T + L_2T^2$).

R		a-axis		c-axis	
		Value	σ	Value	σ
L phase					
Dy	L_0	9.426×10^{0}	2×10^{-3}	1.7642×10^{1}	9×10^{-3}
	L_1	9.0×10^{-5}	8×10^{-6}	1.7×10^{-4}	4×10^{-5}
	L_2	-2.2×10^{-8}	7×10^{-9}	2.2×10^{-7}	3×10^{-8}
Er	L_0	9.431×10^{0}	2×10^{-3}	1.7580×10^{1}	1×10^{-2}
	L_1	8.0×10^{-5}	8×10^{-6}	1.2×10^{-4}	6×10^{-5}
	L_2	-1.6×10^{-8}	6×10^{-9}	3.0×10^{-7}	5×10^{-8}
Ho	L_0	9.434×10^{0}	2×10^{-3}	1.7613×10^{1}	8×10^{-3}
	L_1	9.3×10^{-5}	7×10^{-6}	2.1×10^{-4}	3×10^{-5}
	L_2	-2.6×10^{-8}	6×10^{-9}	2.1×10^{-7}	2×10^{-8}
Tm	L_0	9.409×10^{0}	2×10^{-3}	1.7478×10^{1}	8×10^{-3}
	L_1	5.8×10^{-5}	7×10^{-6}	2.2×10^{-4}	3×10^{-5}
	L_2	–[a]	–[a]	2.2×10^{-7}	2×10^{-8}
Y	L_0	9.430×10^{0}	1×10^{-3}	1.7609×10^{1}	3×10^{-3}
	L_1	7.6×10^{-5}	4×10^{-6}	1.7×10^{-4}	1×10^{-5}
	L_2	-1.2×10^{-8}	3×10^{-9}	2.36×10^{-7}	8×10^{-9}
Yb	L_0	9.400×10^{0}	2×10^{-3}	1.7470×10^{1}	5×10^{-3}
	L_1	6.3×10^{-5}	9×10^{-6}	1.8×10^{-4}	2×10^{-5}
	L_2	–[a]	–[a]	2.4×10^{-7}	2×10^{-8}
H phase					
Dy	L_0	1.3049×10^{1}	4×10^{-3}	9.536×10^{0}	2×10^{-3}
	L_1	1.4×10^{-4}	2×10^{-5}	8.8×10^{-5}	8×10^{-6}
	L_2	1.2×10^{-7}	2×10^{-8}	-7.8×10^{-8}	7×10^{-9}
Eu	L_0	1.3079×10^{1}	8×10^{-3}	9.570×10^{0}	4×10^{-3}
	L_1	1.9×10^{-4}	3×10^{-5}	8.0×10^{-5}	2×10^{-5}
	L_2	1.0×10^{-7}	2×10^{-8}	-6×10^{-8}	1×10^{-8}
Gd	L_0	1.3078×10^{1}	2×10^{-3}	9.576×10^{0}	3×10^{-3}
	L_1	1.9×10^{-4}	1×10^{-5}	4×10^{-5}	1×10^{-5}
	L_2	1.0×10^{-7}	8×10^{-9}	-4×10^{-8}	1×10^{-8}
Ho	L_0	1.3061×10^{1}	2×10^{-3}	9.5451×10^{0}	7×10^{-4}
	L_1	1.4×10^{-4}	1×10^{-5}	9.2×10^{-5}	3×10^{-6}
	L_2	1.3×10^{-7}	8×10^{-9}	-8.5×10^{-8}	3×10^{-9}
Sm	L_0	1.3095×10^{1}	6×10^{-3}	9.576×10^{0}	4×10^{-3}
	L_1	1.9×10^{-4}	3×10^{-5}	8.0×10^{-5}	2×10^{-5}
	L_2	1.1×10^{-7}	2×10^{-8}	-7.0×10^{-8}	2×10^{-8}
Tb	L_0	1.3059×10^{1}	3×10^{-3}	9.565×10^{0}	2×10^{-3}
	L_1	1.9×10^{-4}	1×10^{-5}	6.4×10^{-5}	9×10^{-6}
	L_2	9.0×10^{-8}	9×10^{-9}	-6.7×10^{-8}	7×10^{-9}

Note: Note that the ATEC can be expressed by $\alpha = 1/L_0\, dL/dT = 1/L_0\,(L_1 + L_2T)$.
[a]The 2nd order coefficients, L_2, for the a-axis of Tm and Yb are meaningless. As shown in Figure 5, they show an almost linear line.

$dL/dT|_T$) of the *a*- and *c*-axis were calculated using the coefficients of L_0, L_1 and L_3.

Results

Sample and thermal analysis

The prepared sample powders were generally white in color except for the samples with R = Er, which was pink, R = Tb, which was brownish, and R = Ho, which was orange. No significant signals that indicate weight increase or decrease were observed in the TG analysis for all the samples, and the endothermic/exothermic peaks of melting, solidification, or phase transition were observed in the DTA signals.

The obtained melting temperatures for $Ba_3RB_3O_9$ compounds (R = Sm–Yb, and Y) were summarized in Figure 2. They are consistent with the reported values of melting temperature for R = Dy–Yb and Y by Cox et al. [2], R = Y by Li et al. [4, 5], and R = Tm and Yb by Khamaganova et al. [3], but are inconsistent with those reported for R = Y, Ho, and Er by Khamaganova et al. [3]. It may be noted that the melting temperatures observed during the cooling-down period are different from those during the heating-up period, and the difference reached ~100 °C for Dy, in particular. The fact suggests the overcooled state during the cooling-down period. Additionally, the phase transition temperatures fluctuated in each measurement, suggesting the association of thermal hysteresis or kinetics.

X-ray diffraction measurements

The XRD profiles at RT revealed that the samples with R = Sm–Tb and with R = Dy–Yb, Y showed the H type structures and the L type structures, respectively. In the HT-XRD, no phase transition was found for the H-type phase ($R\bar{3}$) with R = Sm–Tb (Figure 3(a)) and the L-type phase ($P6_3$ cm) with R = Tm–Yb (Figure 3(c)). On the other hand, phase transition from the L phase to the H phase was observed for R = Dy–Er, and Y at around 1,100–1,200 °C (Figure 3(b)). It may be noted that the HT-XRD measurement with R = Dy and Ho did not show phase transition from the H phase to the L phase during the cooling-down period, in particular. The phase transitions for $Ba_3DyB_3O_9$ and $Ba_3HoB_3O_9$ are affected largely by thermal hysteresis or kinetics.

Discussions

The unit cell parameters at room temperature

Figure 4 shows the cell parameters at RT as a function of $r_R + r_O$ (the sum of the effective ionic radius of REE, r_R, and that of oxygen, r_O [12]). The *c*-axis of the L phase increases significantly with increasing $r_R + r_O$, which is associated with the structural features of the L-phase. The L type structure consists of the stacking the RO_6 layers and BaO_9 layers along the *c*-axis and the RO_6 and BaO_9 coordination polyhedra link together by sharing a

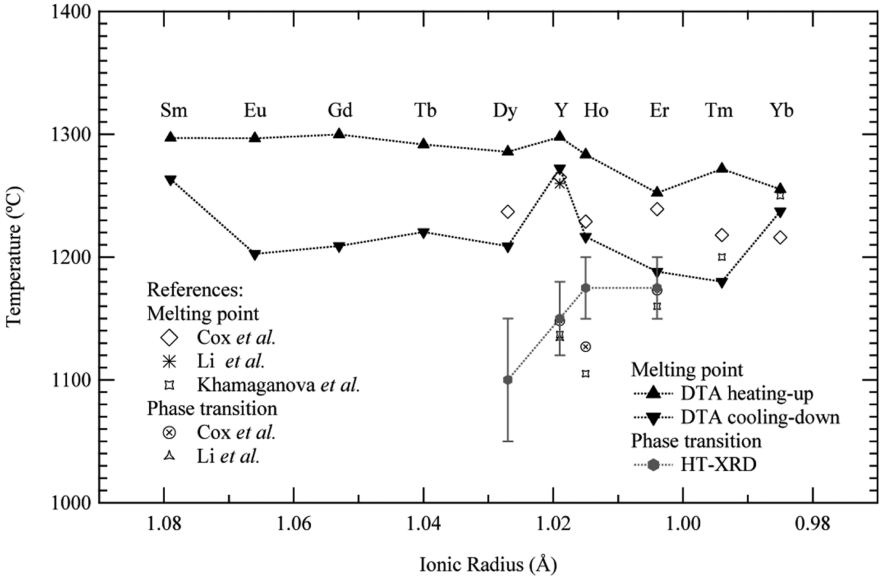

Figure 2: Melting temperatures during heating-up and cooling-down period by DTA and phase transition temperatures during heating-up period by HT-XRD for the $Ba_3RB_3O_9$ system are shown with the published temperatures [2–5]. The horizontal axis is the effective ionic radius of REE [12].

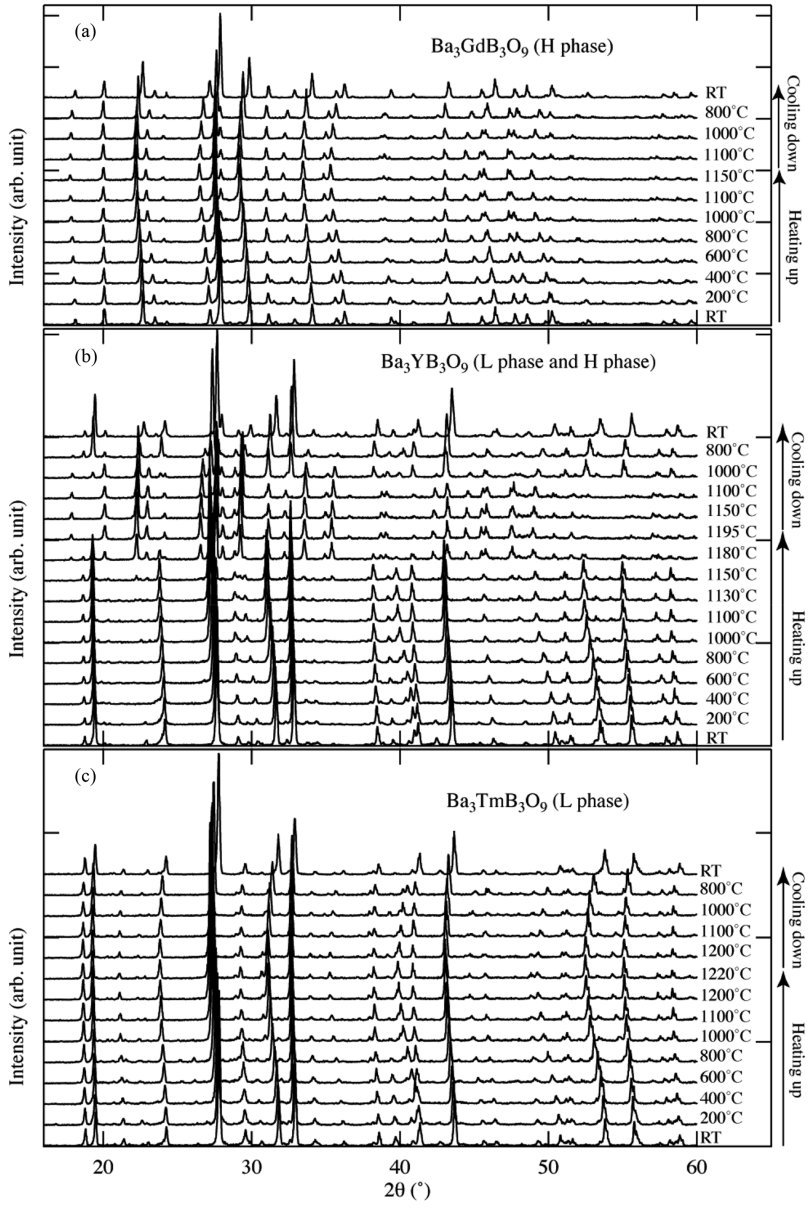

Figure 3: Representative patterns from the three types of typical XRD diffractions for $Ba_3RB_3O_9$; (a) H phase only, R = Gd; (b) H and L phase, R = Y; and (c) L phase only R = Tm. The numbers in the graph show the measurement temperature and RT indicates room temperature.

triangle face. This unique linkage indicates a strong electrostatic repulsion along the *c*-axis and produces an appreciated effect of the length of the *c*-axis. In contrast, the no strong anisotropy was detected in the variation of cell parameters for the H phase as shown in Figure 4(a) and (b). These features are associated with the rather homogeneous arrangement of the RO_6 and BaO_9 polyhedra in the H-type structure.

Thermal expansion coefficients

Temperature dependences of unit cell parameters are shown in Figure 5, and the data can be approximated by quadratic curves.

In the case of the H phase, the ATEC of the *a*-axis increases linearly from ~15×10^{-6} °C^{-1} to ~30×10^{-6} °C^{-1} and that of the *c*-axis decreases linearly from ~10×10^{-6} °C^{-1} to ~ -10×10^{-6} °C^{-1} as a function of temperature. This anisotropic thermal expansion for the H phase can be attributed to the distribution of BO_3 triangles and their thermal vibration at the high temperature [13–16]. The normal vectors of BO_3 triangles are almost perpendicular to the *c*-axis, as shown in the close-up figure of the H phase (Figure 6(a)) and then the expected thermal vibration of BO_3 triangles perpendicular to the plane of the triangle encourages the larger ATEC of the *a*-axis in the present case.

On the contrary, the ATEC for the *a*-axis of the L phase decreases linearly from ~10×10^{-6} °C^{-1} to ~5×10^{-6} °C^{-1} with

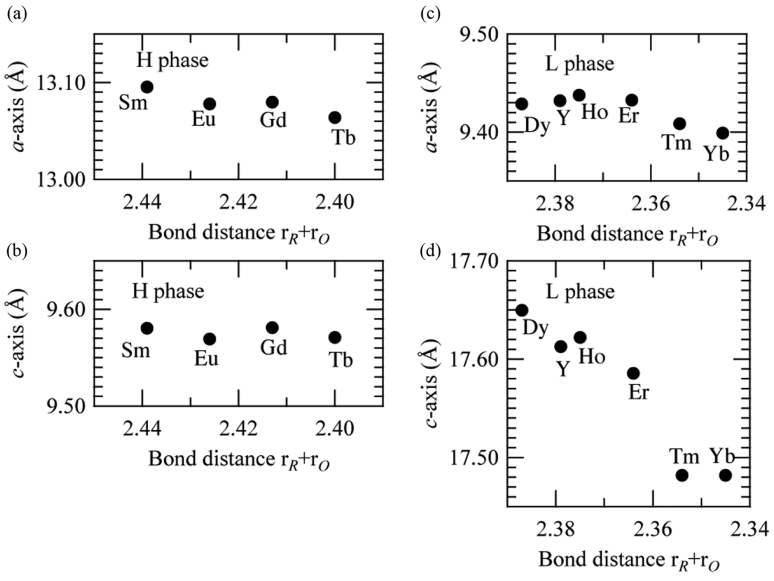

Figure 4: The unit cell parameters versus the sum of the effective ionic radius ratio, $r_R + r_O$, at room temperature; (a) *a*- and (b) *c*-axes of the H phase, and (c) *a*- and (d) *c*-axes of the L phase. Note that horizontal axes are reversed.

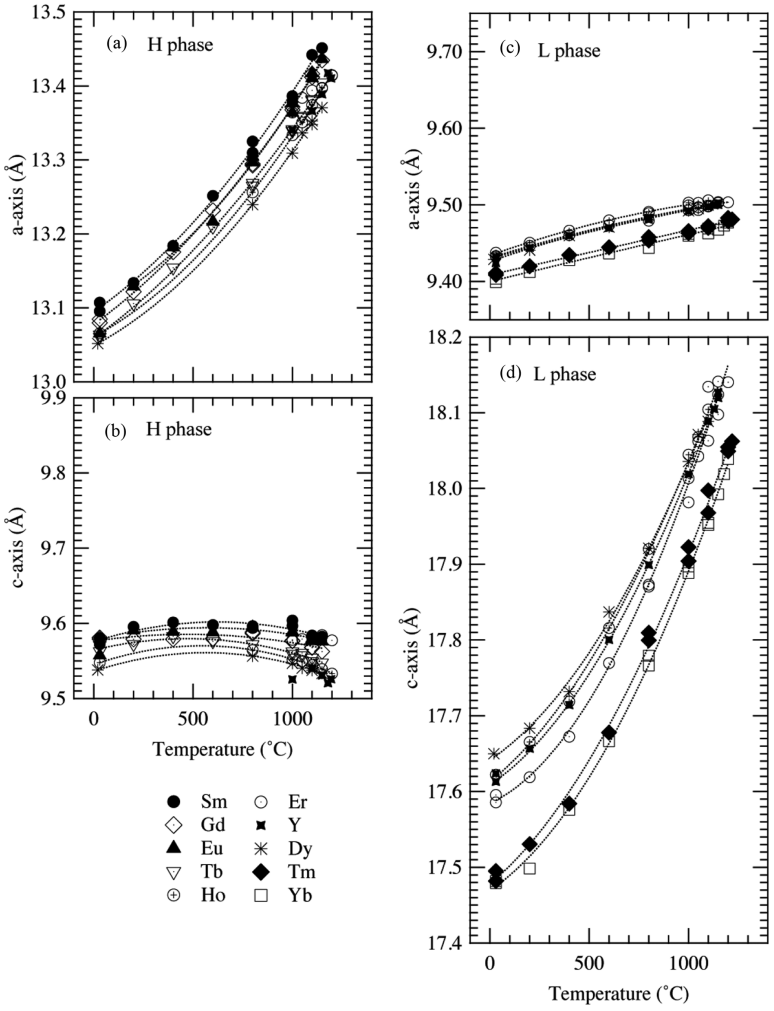

Figure 5: Temperature dependence of the unit cell parameters; (a) *a*- and (b) *c*-axes of the H phase, and (c) *a*- and (d) *c*-axes of the L phase. Dotted lines are the fitted quadratic curves. Fitted coefficients are shown in Table 1.

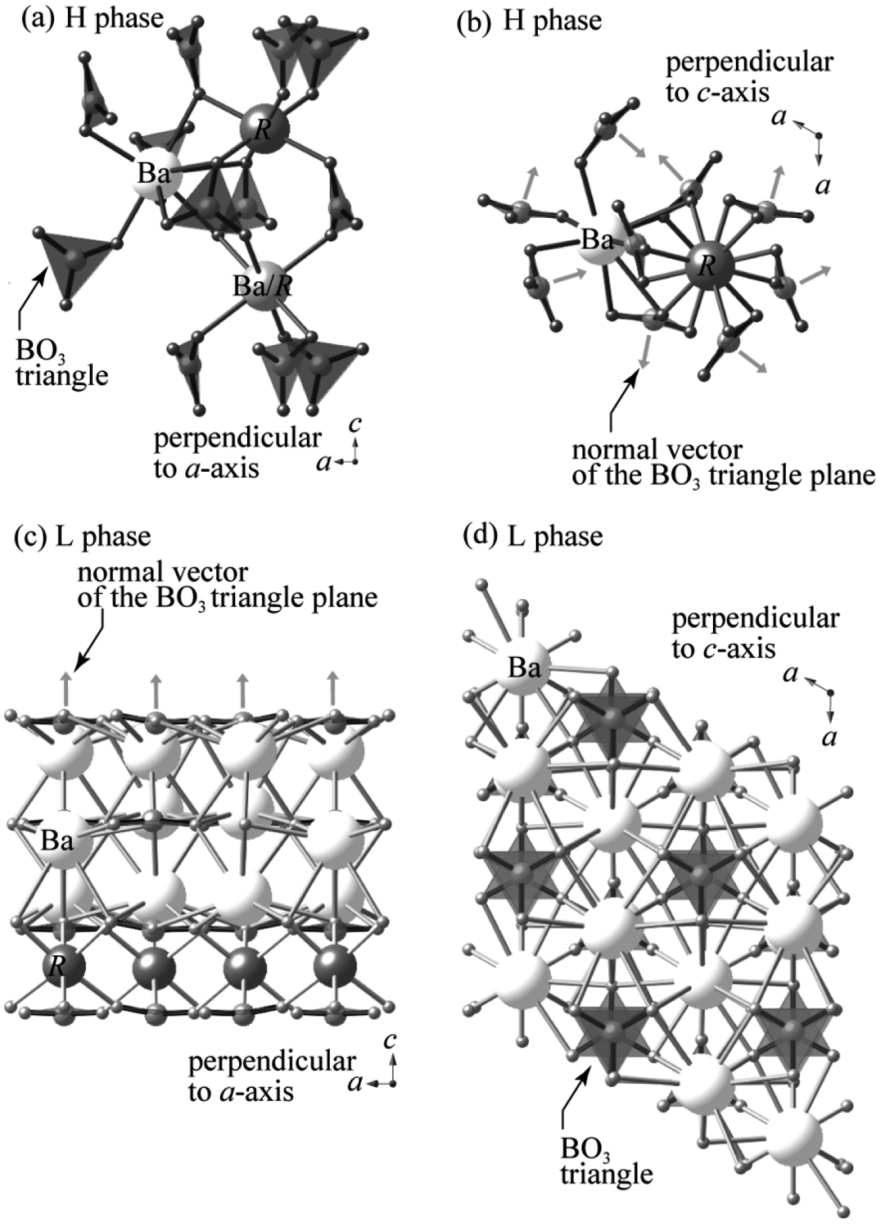

Figure 6: Crystal structure of $Ba_3RB_3O_9$ focused on the direction of the BO_3 triangles illustrated in black triangles. Structures perpendicular to the (a) *a*- and (b) *c*-axes of the H phase and those perpendicular to the (c) *a*- and (d) *c*-axes of the L phase are shown.

increasing temperature, and increases linearly from ~10×10^{-6} °C^{-1} to ~40×10^{-6} °C^{-1} for the *c*-axis. This anisotropy can be discussed by using the structural features found in the alignment of BO_3 triangles, again. As shown in Figure 6, the planes of BO_3 triangles are perpendicular to the *c*-axis, and the anisotropic thermal vibration of the BO_3 triangle could be associated with the larger ATEC along the *c*-axis. Similar distribution of BO_3 triangles was also reported in the structure of $LuBO_3$ (calcite modification), and the larger thermal expansion perpendicular to the BO_3 triangles was demonstrated [13].

Summary

Features of the phase transition in the $Ba_3RB_3O_9$ (R = Sm–Yb, and Y) systems were examined using TG-DTA and HT-XRD. The $Ba_3RB_3O_9$ (R = Sm–Tb) system with the lighter REE indicates no solid–solid phase transition and remained as the H phase up to the melting temperature. The system (R = Tm–Yb) with heavier REE also indicates no solid–solid phase transition, and they remained as the L phase. In contrast, the system (R = Dy–Er, and Y) shows a solid–solid phase transition from L-type to H-type phases.

Features of the thermal expansion coefficient for the $Ba_3RB_3O_9$ (R = Sm–Yb, and Y) systems were investigated by the HT-XRD measurements. The ATEC of the a-axis for the H phase was larger than that of the c-axis. On the contrary, the ATEC of the c-axis for the L phase was larger than that of the a-axis. These anisotropic thermal behaviors are associated well with the systematic distribution of the BO_3 triangles in the crystal structures. The larger thermal expansion is realized in the direction perpendicular to the planes of BO_3 triangles and this feature is in accordance with the thermal vibration of BO_3 triangle.

Acknowledgements: One of the authors (R.S.) was supported by a Grant-in-Aid for Young Scientists (B) (2376003) from the Japan Society for the Promotion of Science (JSPS).

References

[1] A.B. Ilyukhim, B.F. Dzhurinskii and R.J. Inorg. Chem., 38 (1993) 1625–1630.
[2] J.R. Cox, D.A. Keszler and J. Huang. Chem. Mater., 6 (1994) 2008–2013.
[3] T.N. Khamaganova, N.M. Kuperman and Zh.G. Bararova, J. Solid State Chem., 145 (1999) 33–36.
[4] X.Z. Li, X.L. Chen, L. Wu, Y.G. Cao, T. Zhou and Y.P. Xu. J. Alloys Compd., 370 (2004) 53–58.
[5] X.Z. Li, X.L. Chen, J.K. Jian, L. Wu, Y.P. Xu and Y.G. Gao, J. Solid State. Chem., 177 (2004) 216–220.
[6] S. Pan, Z. Hu, Z. Lin and G. Wang. J. Cryst. Growth, 247 (2003) 452–456.
[7] S. Pan, Z. Hu, Z. Lin and G. Wang. J. Cryst. Growth, 263 (2004) 214–217.
[8] B. Han, H.B. Liang, H.H. Lin, J.P. Zhong, Q. Su, P. Dorenbos, M. Danang-Birowosuto, G.B. Zhang and Y.B. Fu. J. Appl. Phys., 101 (2007) #113530.
[9] R. Sole, F. Guell, J. Gavalda, M. Aguilo and F. Diaz. J. Mater. Res., 23 (2008) 2512–2518.
[10] R. Simura, T. Yagi, K. Sugiyama, T. Yanagida and A. Yoshikawa. J. Cryst. Growth, 362 (2013) 145–158.
[11] T. Mitsunaga, M. Saigo and G. Fujinawa. Powder Diffr., 17 (2002) 173–177.
[12] R.D. Shannon. Acta Cryst. A., 32 (1976) 751–767.
[13] S.K. Filatov and R.S. Bubnova. Phys. Chem. Glasses: Eur. J. Glass Sci. Technol. B, 56 (2015) 24–35.
[14] W.-D. Stein, A. Cousson, P. Becker, L. Bohaty and M. Braden, Z. Kristallogr., 222 (2007) 680–689.
[15] R.S. Bubnova and S.K. Filatov. Phys. Status Solid., 245 (2008) 2469–2476.
[16] S.N. Volkov, S.K. Filatov, R.S. Bubnova, V.L. Ugolkov, T.N. Ugolkov, T.N. Svetlyakova and A.E. Kokh. Glass Phys. Chem., 38 (2012) 162–177.